RSC Publishing Faraday Discussions

Quantifying Photothermal Heating at Plasmonic Nanoparticles by Scanning Electrochemical Microscopy

Journal:	*Faraday Discussions*
Manuscript ID	FD-ART-03-2018-000057
Article Type:	Paper
Date Submitted by the Author:	05-Mar-2018
Complete List of Authors:	Yu, Yun; Temple University, Chemistry Williams, Jeffrey; Temple University, Chemistry Willets, Katherine; Temple University, Chemistry

Faraday Discussions

ARTICLE

Quantifying Photothermal Heating at Plasmonic Nanoparticles by Scanning Electrochemical Microscopy

Yun Yu, Jeffrey D. Williams, and Katherine A. Willets*

Photothermal heating at metal nanoparticles results from the non-radiative decay of localized surface plasmons. The local heat generation enhances the mass transport rate of redox molecules and causes a shift in their formal potential, both of which can impact an electrochemical process at the nanoparticle interface. Here we present a methodology for probing the surface temperature at a plasmonic nanoparticle substrate using scanning electrochemical microscopy (SECM). Light is used to excite a plasmonic substrate electrode, while an ultramicroelectrode tip is positioned close to the substrate to read out both the mass transfer rate and concentration profile of the redox molecules. The measured mass transfer rate and the shift in the equilibrium potential provide a quantitative value of the temperature increase at the substrate surface, which is verified by simulations using a mass transfer model coupled with heart dissipation. The developed SECM approach is suitable for probing heat generation at a variety of both plasmonic and non-plasmonic nanostructures.

Introduction

Metal nanoparticles with high free-electron mobility (Au, Ag, *etc)* are capable of supporting localized surface plasmons, which are collective oscillations of surface conduction electrons driven by an electromagnetic radiation (*e.g.* light).[1-3] Plamons decay either radiatively through re-emitted photons[4] or non-radiatively via electron–electron and electron–phonon collisions, and the absorbed photon energy converts to heat.[5, 6] The heat is dissipated from the particles into the surrounding environment and results in an increase of the local temperature (Figure 1A). The energy conversion and heat dissipation processes can be readily used for targeted heating of species near the nanoparticles, and has been successfully adopted in applications such as photothermal therapy[7, 8], energy harvesting[9, 10], and optoelectronic devices[11]. The heating efficiency is often affected by the intensity, wavelength, and polarization of the radiation source, and the geometry of the plasmonic structures[1, 2]. The ability to measure the resulting local temperature is of importance for designing efficient photothermal devices. To date, a variety of techniques have been employed for characterizing the thermal properties of the plasmonic structures, such as scanning thermal microscopy[6], quadriwave shearing interferometry[5], surface-enhanced Raman scattering[12], resistance measurements[13], and thermographic phosphors[14].

Herein we demonstrate an electrochemical approach to probe the photothermal heating at an illuminated plasmonic substrate using scanning electrochemical microscopy (SECM). The electro-active nature of the plasmonic metal nanoparticles allows heterogeneous electron-transfer reactions to take place at the particle-solution interface. The photothermal effects of the plasmonic nanoparticles can impact the electrochemical process, including enhancing the mass transport rate of the redox molecules and causing a shift in the equilibrium potential of the nanoparticle electrode, both of which can be probed by SECM.[15] SECM has been previously employed for probing electrocatalysis[16-18], photoelectrochemical processes[19-22], as well as the thermal conductivity of materials[23]. In an SECM experiment, an ultramicroelectrode (UME) or nanoelectrode employed as a tip is brought close to a region of interest of a substrate. As depicted in Figure 1B, a potential applied to the tip electrode (E_T) that is significantly negative relative to the standard potential of the redox probe (E^0) leads to the reduction of the oxidized form of the probe (O) to its reduced form (R) at a diffusion-limited rate. Measuring the reduction current at the tip electrode (i_T) allows us to monitor the products of oxidation reactions occurring at the substrate surface. Rapid diffusion and heat transfer

Department of Chemistry, Temple University, Philadelphia, Pennsylvania 19122, United States. Email: kwillets@temple.edu
Electronic Supplementary Information (ESI) available: Response of bare ITO, Au deposited on glass, Ruthenium(III) hexamine, electrochemical data at different temperatures, and description of simulations. See DOI: 10.1039/x0xx00000x

within the gap between the tip and substrate electrode allows us to obtain the steady-state electrochemical response at the illuminated region of the substrate. The plasmonic substrate used in this work is prepared by depositing Au nanoparticles (5-20 nm) onto indium tin oxide (ITO) coated glass coverslips by thermal evaporation (see Experimental Section for details). A 532-nm laser is introduced through a 1.45 NA 60× objective of an inverted optical microscope to excite an area ~70 μm in diameter at substrate (Figure 1B). Upon plasmon excitation, the heat transfer from the Au to the solution results in enhanced mass transfer rates of the redox molecules to the tip electrode. Moreover, the thermal-induced shift in the formal potential of the redox molecules results in a potential difference between the local equilibrium potential and the substrate potential, thus leading to electrochemical reactions occurring at the substrate.[15] Both of the effects can impact the current measured at the tip electrode positioned at the laser spot. By controlling the potentials applied to both the substrate and tip electrodes, we obtain the electrochemical response from different redox mediators that allows us to probe and quantify the photothermal heating at the plasmonic substrate.

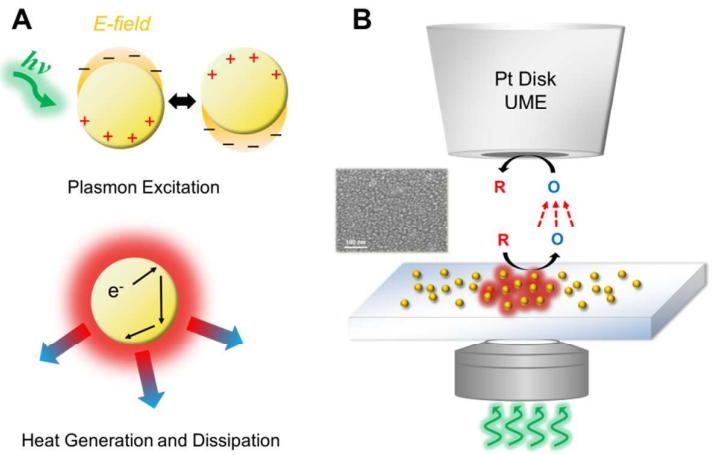

Figure 1 (A) Scheme showing excitation of surface plasmons (top) and heat generation at a plasmonic nanoparticle surface (bottom). (B) Schematic representation of an SECM setup integrated with an optical microscope. The inset shows the SEM image of an Au nanoparticle substrate.

Experimental

Chemicals. Potassium hexacyanoferrate (II) trihydrate ($K_4Fe(CN)_6 \cdot 3H_2O$, 99.95%), potassium ferricyanide ($K_3Fe(CN)_6$, 99%), hexaammineruthenium(III) chloride ($Ru(NH_3)_6Cl_3$, 98%), and potassium chloride (KCl, 99%) were purchased from Sigma-Aldrich and used as received. All aqueous solutions were prepared using nanopure water from an arium pro ultrapure water system (Sartorius).

Substrate Preparation and Characterization. Au nanoparticles supported by ITO or glass were prepared by thermal evaporation. ITO-coated glass coverslips (15–30 Ω, SPI Supplies) or glass coverslips (Fisher Scientific) were cleaned inside an argon plasma cleaner (PDC-32G, Harrick plasma) for 10 min. Gold (99.95%, Ted Pella, Inc.) was thermally evaporated and deposited (Nano 36, Kurt J. Lesker) onto the cleaned ITO or glass surface at a rate of 0.5 Å/s to a final thickness of 10 nm. A copper wire was attached to the ITO with silver epoxy (MG Chemicals) for electrical contact. A Quanta 450 FEG scanning electron microscope (SEM) was used to image the morphology of the Au film.

Electrochemical and SECM Setup. Pt disk UME/nanoelectrodes were prepared by pulling and heat sealing 25 μm-diameter Pt wires (Goodfellow) into borosilicate glass capillaries with a P-2000 laser pipette puller (Sutter Instrument Co.) and polishing under video microscopic control, as described previously.[15] All electrochemical measurements were performed using a CH750E bipotentiostat (CH Instruments). A Pt wire and an Ag wire coated with AgCl were used as a counter and reference electrode respectively. The tip electrode was positioned close to the transparent substrate using a stepper motor (Microdrive, Mad City Labs Inc.). The process is continuously monitored with an inverted optical microscope (Olympus IX-73). A 532-nm laser (Spectra-Physics, 532−50-CDRH) was introduced through a 1.45 NA

60× oil immersion objective (Olympus PlanoApo N) to excite the Au substrate. The laser was chopped with a controlled frequency using a mechanical shutter (Uniblitz Electronic).

Finite Element Simulation. The finite element simulations were performed using COMSOL Multiphysics v5.2a (COMSOL) to model the tip current response. Simulation details are provided in the Supplementary Information.

Results and discussion

For the first set of experiments, we probe the effect of photothermal heating on mass transport between the substrate and tip. We use a well-defined, one-electron transfer, reversible redox couple, $Fe(CN)_6^{3-}$ (O) and $Fe(CN)_6^{4-}$ (R), as the redox mediator, and the solution contains both forms of the species at equal concentrations. The steady-state, mass-transport-limited anodic tip currents ($i_{a,\infty}$) and cathodic tip currents ($i_{c,\infty}$) at highly oxidizing ($E_T >> E^0$) or reducing ($E_T << E^0$) tip potentials are a function of both the mass transport coefficient and the local concentration of reactant, as given by Equations 1 and 2 below[24],

$$i_{a,\infty} = FAm_R c_R^* \quad (1)$$

$$i_{c,\infty} = FAm_O c_O^* \quad (2)$$

Here F is the Faraday constant, A is the area of the tip electrode, m_O and m_R are the mass transfer coefficients of O and R, respectively, and c_O^* and c_R^* are the bulk concentrations of O and R, respectively. We use $i_{a,\infty}$ and $i_{c,\infty}$ as metrics to quantify the mass transfer rate, as well as the concentration profile of the redox molecules. The substrate generation-tip collection (SG/TC) experiments were first carried out as depicted in Figure 2A. In this mode, the potential at the plasmonic substrate (E_S) is either much higher or lower than E^0, *e.g.* biasing the Au substrate at a high reducing potential (E_S =0V *vs* Ag/AgCl) results in the reduction of O at the Au surface with a diffusion-controlled rate. Under this condition, the steady-state voltammogram obtained by sweeping the tip potential using a 490-nm-radius Pt UME positioned 10 μm from the substrate contains only an oxidation wave, due to the complete depletion of O near the substrate (black curve in Figure 2B). Upon illumination using a 400 W/cm^2 532-nm laser, the magnitude of the anodic diffusion limiting current ($i_{a,\infty}$) at the tip increases from 554 pA to 736 pA (red curve in Figure 2B). Because O is depleted at the substrate, we assign the source of the ~33% current enhancement as originating from enhanced mass transport due to local heating[15].

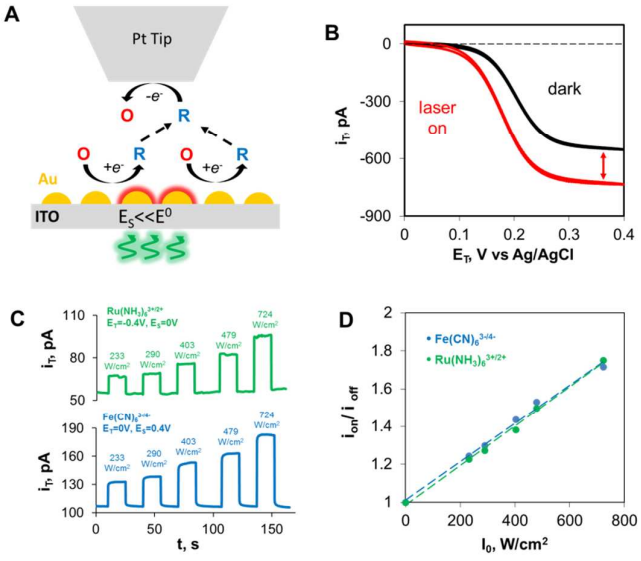

Figure 2 (A) Schematic representation of an SECM generation-collection experiment with the substrate biased for diffusion-controlled reduction. (B) Steady-state voltammograms of $Fe(CN)_6^{3-/4-}$ obtained with a 490-nm-radius Pt UME before (black) and after (red) 400 W/cm^2 illumination at the substrate. E_S=0 V. Scan rate is 50 mV/s. (C) Current *vs* time trace obtained with a 95-nm-radius Pt electrode in 2mM $Fe(CN)_6^{3-/4-}$ solution with E_T=0V, E_S=0.4V (blue) and in 2mM $Ru(NH_3)_6^{3+}$ solution with E_T=-0.4V, E_S=0V (green) at different excitation intensities. The light is switched on for 15 seconds at the indicated intensity, then off for 15 seconds. (D) Plots of i_{on}/i_{off} *vs* laser intensity for $Fe(CN)_6^{3-/4-}$ (blue) and $Ru(NH_3)_6^{3+/2+}$ (green). The tip-substrate distance is 10 μm. All solutions contain 0.5 M KCl.

Next we investigate the effects of the laser intensity (I_0) on the enhanced mass transport due to plasmon-induced heating at the Au substrate. The substrate is biased at 0.4 V *vs* Ag/AgCl to deplete R near the substrate, while the tip electrode is biased at 0 V to collect O. The time trace of i_T obtained with a 95-nm-radius Pt nanoelectrode at different laser intensities is shown as the blue curve in Figure 2C. Higher laser intensity results in higher i_T, as expected. The effect of heating on the measured current at the tip is quantified as the ratio of i_T with and without substrate illumination (i_{on}/i_{off}). The blue curve in Figure 2D shows a plot of i_{on}/i_{off} *vs.* laser intensity and reveals a linear dependence on the illumination intensity at 532 nm. For comparison, similar experiments are performed using $Ru(NH_3)_6^{2+/3+}$ as the redox couple. The substrate is biased at 0 V to deplete R ($Ru(NH_3)_6^{2+}$) while E_T= -0.4 V is applied to the tip for diffusion-controlled reduction of O ($Ru(NH_3)_6^{3+}$). The i_T response at different intensities is shown as the green curve in Figure 2C. The intensity dependence of i_{on}/i_{off} is shown in Figure 2D (green curve), which is essentially identical to that of $Fe(CN)_6^{3-/4-}$. The data obtained from two different redox species both suggest that the mass transfer rate of the redox molecules to the tip electrode increases between 22%-75% with an excitation intensity range of 233-724 W/cm^2.

In the next set of experiments, the substrate bias is at open circuit (O.C.), allowing plasmon-induced heating to affect both the mass transport rate and the local concentration of the redox couple[15] (Figure 3A). The tip voltammogram obtained with a 490-nm Pt UME positioned 10 μm from the substrate contains both an oxidation and a reduction wave (black curve in Figure 3B) in a solution containing equal concentrations of $Fe(CN)_6^{3-}$ and $Fe(CN)_6^{4-}$. The magnitudes of $i_{c,\infty}$ and $i_{a,\infty}$ in the non-illuminated case are approximately same, and the minor difference is due to the ratio of the diffusion coefficients of the two forms D_R/D_O=0.92[25]. Upon illumination, we find a significant increase in the magnitude of the reduction wave, but a slight decrease in the magnitude of the oxidation wave (red curve in Figure 3B). The change in the ratio of the two waves when the light is on *vs.* off suggests that in addition to increased mass transport, there is also an increase of local c_O and a decrease of local c_R, which we assign to a photo-induced oxidation reaction at the substrate[15], as illustrated in Figure 3A. We also note that a conductive substrate is necessary for photo-induced oxidation to proceed, by allowing charge to be transferred from the Au to the external circuit and permitting electron-transfer reactions (Figure S1).

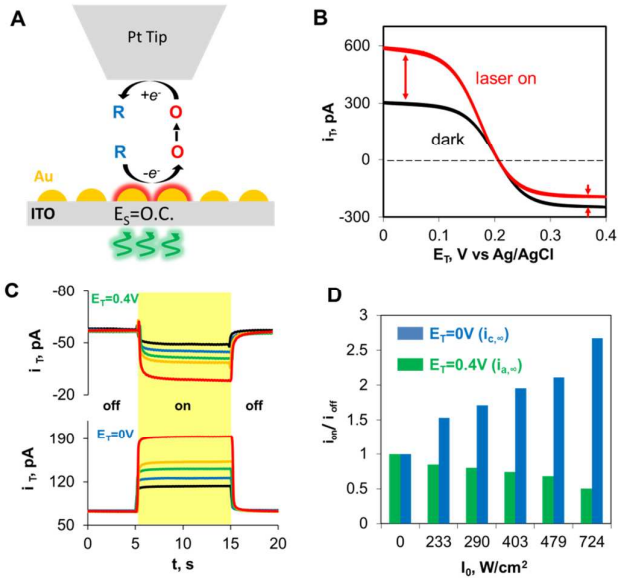

Figure 3 (A) Schematic representation of an SECM generation-collection experiment with substrate at open circuit. (B) Steady-state voltammograms of $Fe(CN)_6^{3-/4-}$ obtained with a 490-nm-radius Pt UME before (black) and after (red) 400 W/cm^2 illumination at the substrate. Substrate is at open circuit. Scan rate is 50 mV/s. (C) Current *vs* time trace obtained with a 110-nm-radius Pt tip with E_T=0.4V and E_S = O.C. (upper curves), and E_T=0V, E_S=O.C. (lower curves). The laser was switched on at t = 5s and off at t = 15s. The laser intensities were 724 W/cm^2 (red), 479 W/cm^2 (orange), 403 W/cm^2 (green), 290 W/cm^2 (blue) and 233 W/cm^2 (black). (D) Plot of i_{on}/i_{off} for $i_{c,\infty}$ (blue) and $i_{a,\infty}$ (green). Solution contains 2mM $Fe(CN)_6^{3-}$, 2mM $Fe(CN)_6^{4-}$ and 0.5M KCl. The tip electrode is placed 10 μm from the substrate.

Figure 3C shows the time traces of $i_{a,\infty}$ (E_T=0.4V) and $i_{c,\infty}$ (E_T=0V) with the substrate at open-circuit while a 110-nm-radius tip is positioned 10 μm away from the substrate. The trends in i_{on}/i_{off} with E_T=0V and E_T=0.4V at different laser intensities are shown in Figure 3D. As the laser intensity increases, $i_{c,\infty}$ (E_T =0 V) increases monotonically, and the magnitude of the current change is higher than what was observed in Figure 2D. This is due to the synergistic effects of the photo-induced oxidation and local heating, which increase both c_O and m_O, respectively. Alternatively, the $i_{a,\infty}$ (E_T =0.4 V) in Figure 3D decreases monotonically as a function of laser intensity, due to the competition between the light-driven increase in m_R and decrease in c_R. The overall decrease in the anodic current as the laser intensity increases shows that the increase in m_R is dominated by the decrease in c_R.

Because the tip current is affected by both enhanced mass transport and light-induced oxidation at the substrate, the tip current ratio i_{on}/i_{off} is not suitable for quantification of the photo-induced oxidation reaction. Deriving Equation 3 from Equations 1 and 2, we find that the local concentration ratio of the two forms can be evaluated as shown:

$$\frac{c_O}{c_R} = \frac{m_R}{m_O}\frac{i_{c,\infty}}{i_{a,\infty}} \quad (3)$$

The ratio of the mass transport rates of the two species (m_R/m_O=0.92) remains constant.[15] Thus, by comparing the magnitudes of $i_{c,\infty}$ and $i_{a,\infty}$ when the substrate is at open circuit, the effects of photo-induced oxidation can be isolated from the interference of the heating effects on mass transport, and the concentration ratio c_O/c_R can be used for quantification for the photo-induced oxidation. The c_O/c_R ratios at different laser intensities are calculated using *Eq.* 3 and presented in the blue curve in Figure 4A. The c_O/c_R ratio has an exponential dependence with excitation intensity, suggesting that the photo-induced oxidative potential at the substrate is proportional to the laser intensity. Control experiments were performed using a bare ITO coverslip as the substrate, and the change in i_T is ~one order of magnitude lower than that obtained with an Au nanoparticle film under the same irradiation conditions, thus verifying that the response is not significantly affected by the supporting substrate or by laser illumination of the Pt tip electrode (Figure S2). The light absorption by the redox mediators is at much shorter wavelength than that used in the experiments[15] and therefore the current response is only attributed to light absorption by the Au film.

In our previous work, we reported two mechanisms for driving photo-induced reactions at a plasmonic Au nanoparticle substrate: photothermal shifts in the formal potential of the redox couple and plasmon-excited hot carriers.[15] In the case of the former, the E^0 value shifts with temperature due to the entropy change associated with the redox process.[26] For $Fe(CN)_6^{3-/4-}$, the E^0 shifts towards more negative values as the temperature increases with a slope of -1.53 mV/K.[26, 27] Thus, as the temperature increases within the laser spot, the reaction will favor oxidation products. Another mechanism that can lead to the observed photo-induced oxidation is hot-hole photochemistry, in which energetic charge carriers are generated at the Au nanoparticle surface upon plasmon excitation.[28-30] While the electrons are injected into the conductive support (ITO) adjacent to the Au and transferred to the external circuit, the holes remaining at the gold are able to oxidize adsorbed redox molecules.[31, 32] We previously reported that the ratio c_O/c_R will have an exponential dependence on excitation intensity in the case of thermally-mediated enhanced photo-oxidation and a linear dependence on excitation intensity in the case of hot-carrier-induced photo-oxidation. Given that the response of the c_O/c_R ratio for $Fe(CN)_6^{3-/4-}$ in Figure 4A shows an exponential dependence on laser intensity, the data suggests that thermal effects are responsible for the enhanced photo-oxidation at this particular substrate and that hot carriers play a minimal role.

To further verify that thermal effects are the dominant mechanism for enhanced photo-oxidation of the $Fe(CN)_6^{3-/4-}$, we examine the behavior of another redox mediator, $Ru(NH_3)_6^{2+/3+}$ using the same substrate. In contrast to $Fe(CN)_6^{3-/4-}$ which shows a negative shift in E^0 as the temperature increases, the $Ru(NH_3)_6^{2+/3+}$ couple has a positive shift in E^0 with increasing temperature; thus we expect to favor the formation of the reduced form of the molecule as the temperature increases at the substrate. For these experiments, the initial solution only contains the oxidized form, $Ru(NH_3)_6^{3+}$, and thus an E_S=E^0 of $Ru(NH_3)_6^{2+/3+}$ is applied to the substrate to generate equal concentrations of O and R near the substrate before laser illumination. The tip current response at different laser intensities is shown in Figure S3. Using *Eq.* 3 and m_R/m_O=1.09,[33] the c_O/c_R values are evaluated and displayed as the green curve in Figure 4A. In contrast to the response of $Fe(CN)_6^{3-/4-}$ (blue curve), the c_O/c_R decreases monotonically as a function of intensity, suggesting that a photo-induced reduction reaction is taking place at the Au substrate upon plasmon excitation, as predicted.

Next, we quantify the extent to which plasmon excitation generates a local temperature increase at the substrate. The relationship between c_O/c_R and the potential shift, ΔE, can be evaluated based on the Nernst equation (*Eq.* 4),

$$\Delta E = E^0 - E_S = -\frac{RT}{F} ln \frac{c_O}{c_R} \quad (4)$$

In the case of local heating, E^0 changes linearly as the temperature increases, as shown in Figure S4. Because temperature scales linearly with excitation intensity,[5] we expect E^0 to have a linear dependence with excitation intensity. On the other hand, if hot carriers are present, we expect E_S to also change with laser intensity, due to the build-up of hot holes locally within the laser spot, which will result in a non-linear dependence of ΔE with the intensity.[32] The blue and green curves in Figure 4B show the change in ΔE calculated from the measured c_O/c_R values (Figure 4A) for $Fe(CN)_6^{3-/4-}$ and $Ru(NH_3)_6^{2+/3+}$, respectively. The ΔE values for both probe molecules show a linear dependence with intensity, but with slopes of opposite sign and varying steepness, due to their different sensitivities of E^0 to temperature change. Using the temperature coefficients -1.65 mV/K for $Fe(CN)_6^{3-/4-}$ and +0.46 mV/K for $Ru(NH_3)_6^{2+/3+}$ (Figure S4), we obtain the temperature changes at the substrate, ΔT, as shown in the blue and green curves in Figure 4C, respectively. The ΔT *vs* intensity relationships obtained from the two different redox mediators show excellent agreement, suggesting that the photo-induced reactions at Au are entirely due to the thermal-induced potential shift, and the effects of hot charge carriers are trivial at the studied Au substrate. More importantly, this analysis allows us to obtain a quantitative temperature measurement at a plasmonic nanoparticle substrate based on two independent measurements.

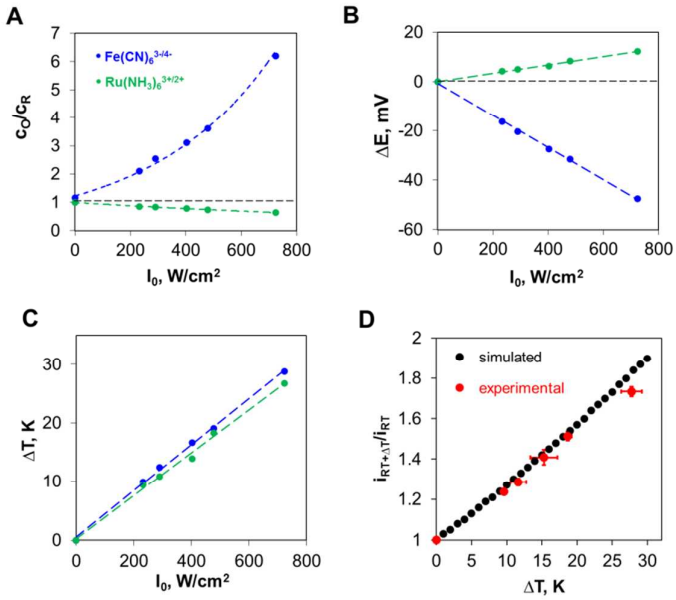

Figure 4 (A) c_O/c_R *vs.* laser intensity relationship of $Fe(CN)_6^{3-/4-}$ (blue) and $Ru(NH_3)_6^{2+/3+}$ (green) and exponential fits. (B) Intensity dependence of ΔE for $Fe(CN)_6^{3-/4-}$ (blue) and $Ru(NH_3)_6^{2+/3+}$ (green) calculated from equation 4 using the c_O/c_R values in panel A. (C) Intensity dependence of ΔT for $Fe(CN)_6^{3-/4-}$ (blue) and $Ru(NH_3)_6^{2+/3+}$ (green) calculated from ΔE values in panel B. (D) Simulated $i_{\Delta T+RT}/i_{RT}$ as a function of ΔT (black) and the experimental data obtained from Figure 2D and 4C (red).

One challenge with the proposed approach for measuring temperatures at plasmonic nanoparticle substrates is that excitation of hot carriers will affect c_O/c_R and E_S, thus preventing us from converting ΔE into an absolute temperature without making some simplifying approximations. However, we recognize that the enhanced mass transport rate, obtained by calculating i_{on}/i_{off} when an overpotential is applied to the substrate (as in Figure 2D), should also contain temperature information that can be used to estimate the substrate temperature and will be independent of hot carrier effects. To do this, a coupled mass transfer and heat transfer mathematical model is used to simulate the tip current response with different ΔT at the illuminated substrate (see Supporting Information for simulation details). The simulated ratio of the tip current at higher temperature ($i_{RT+\Delta T}$) and room temperature (i_{RT}) is shown as the black curve in Figure 4D. For comparison, we also plot the average i_{on}/i_{off} values for the two redox mediators from Figure 2D, converting the intensity to ΔT using the data from Figure 4C. The red data in Figure 4D shows that the average values of i_{on}/i_{off} are in excellent agreement with the simulated $i_{RT+\Delta T}$ / i_{RT} values at the lower temperatures, although some deviation is observed at the highest temperature. We note that our model to simulate the current response is

rather simplified, *i.e.* heating-induced convective flow was not incorporated into the model, and thus we expect even better agreement upon incorporating these effects. Future work will focus on using an improved model for a more accurate estimation of the surface temperature. Nonetheless, the agreement between the predicted temperature based on the increase in photocurrent due to enhanced mass transport (Figure 2D) and the temperature measured by temperature-dependent shifts in the formal potential (Figure 4, B and C) is encouraging, particularly for cases when plasmonic substrates show evidence of both hot carrier and thermal effects, where the latter approach will be impacted by changes in both E_S and E^0.

Conclusions

In this paper, we presented an SECM approach for probing the photothermal heating at a plasmonic nanoparticle substrate and providing a quantitative measurement of the temperature rise due to plasmon excitation. Local heating at the Au nanoparticle substrate results in enhanced mass transfer rates of the redox molecules, as well as a shift in the formal potential of a redox couple, both of which can be quantified by obtaining the tip current response with a suitable potential applied to the tip and substrate electrode. The surface temperature change evaluated from two independent redox probes show excellent agreement with one another and also agree with temperature-dependent simulations of enhanced currents due to increased mass transport rates. The developed method provides an efficient way to quantify the photothermal heating at plasmonic structures. Future directions include using tip electrodes with size comparable to individual nanostructures, which would allow us to probe the surface temperature at individual plasmonic nanoparticles.

Conflicts of interest

There are no conflicts to declare.

Acknowledgements

The support of this work by the AFOSR MURI (FA9550-14-1-0003) is gratefully acknowledged.

Notes and references

1 K. A. Willets and R. P. V. Duyne, *Annu. Rev. Phys. Chem.*, 2007, **58**, 267-297.

2 K. M. Mayer and J. H. Hafner, *Chem. Rev.*, 2011, **111**, 3828-3857.

3 S. Zeng, D. Baillargeat, H.-P. Ho and K.-T. Yong, *Chem. Soc. Rev.*, 2014, **43**, 3426-3452.

4 C. Sönnichsen, T. Franzl, T. Wilk, G. von Plessen, J. Feldmann, O. Wilson and P. Mulvaney, *Phys. Rev. Lett.*, 2002, **88**, 077402.

5 G. Baffou, P. Berto, E. Bermúdez Ureña, R. Quidant, S. Monneret, J. Polleux and H. Rigneault, *ACS Nano*, 2013, **7**, 6478-6488.

6 B. Desiatov, I. Goykhman and U. Levy, *Nano Lett.*, 2014, **14**, 648-652.

7 D. Jaque, L. Martinez Maestro, B. del Rosal, P. Haro-Gonzalez, A. Benayas, J. L. Plaza, E. Martin Rodriguez and J. Garcia Sole, *Nanoscale*, 2014, **6**, 9494-9530.

8 L. R. Hirsch, R. J. Stafford, J. A. Bankson, S. R. Sershen, B. Rivera, R. E. Price, J. D. Hazle, N. J. Halas and J. L. West, *Proc. Natl. Acad. Sci. U.S.A*, 2003, **100**, 13549-13554.

9 O. Neumann, A. S. Urban, J. Day, S. Lal, P. Nordlander and N. J. Halas, *ACS Nano*, 2013, **7**, 42-49.

10 O. Neumann, C. Feronti, A. D. Neumann, A. Dong, K. Schell, B. Lu, E. Kim, M. Quinn, S. Thompson, N. Grady, P. Nordlander, M. Oden and N. J. Halas, *Proc. Natl. Acad. Sci. U.S.A*, 2013, **110**, 11677-11681.

11 L. Vicarelli, M. S. Vitiello, D. Coquillat, A. Lombardo, A. C. Ferrari, W. Knap, M. Polini, V. Pellegrini and A. Tredicucci, *Nat. Mater.*, 2012, **11**, 865.

12 H. Yang, L.-Q. He, Y.-W. Hu, X. Lu, G.-R. Li, B. Liu, B. Ren, Y. Tong and P.-P. Fang, *Angew. Chem. Int. Ed.*, 2015, **54**, 11462-11466.

13 J. B. Herzog, M. W. Knight and D. Natelson, *Nano Lett.*, 2014, **14**, 499-503.

14 Z. J. Coppens, W. Li, D. G. Walker and J. G. Valentine, *Nano Lett.*, 2013, **13**, 1023-1028.

15 Y. Yu, V. Sundaresan and K. A. Willets, *J. Phys. Chem. C*, 2018, DOI: 10.1021/acs.jpcc.7b12080.

16 T. Sun, Y. Yu, B. J. Zacher and M. V. Mirkin, *Angew. Chem. Int. Ed.*, 2014, **53**, 14120-14123.

17 P. Bertoncello, *Energy Environ. Sci.*, 2010, **3**, 1620-1633.

18 J. Kim, C. Renault, N. Nioradze, N. Arroyo-Currás, K. C. Leonard and A. J. Bard, *J. Am. Chem. Soc.*, 2016, **138**, 8560-8568.

19 F. Conzuelo, K. Sliozberg, R. Gutkowski, S. Grützke, M. Nebel and W. Schuhmann, *Anal. Chem.*, 2017, **89**, 1222-1228.

20 M. R. Krumov, B. H. Simpson, M. J. Counihan and J. Rodríguez-López, *Anal. Chem.*, 2018, DOI: 10.1021/acs.analchem.7b04896.

21 S. Lhenry, B. Boichard, Y. R. Leroux, P. Even-Hernandez, V. Marchi and P. Hapiot, *Phys. Chem. Chem. Phys.*, 2017, **19**, 4627-4635.

22 D. Zigah, J. Rodriguez-Lopez and A. J. Bard, *Phys. Chem. Chem. Phys.*, 2012, **14**, 12764-12772.

23 A. Boika and Z. Zhao, *Electrochem. Commun.*, 2016, **68**, 36-39.

24 A. J. Bard and L. R. Faulkner, *Electrochemical Methods: Fundamentals and Applications, 2nd Edition*, Wiley, New York, 2001.

25 Y. Yu, T. Sun and M. V. Mirkin, *Anal. Chem.*, 2016, **88**, 11758-11766.

26 U. Kumar Sur, F. Marken, N. Rees, B. A. Coles, R. G. Compton and R. Seager, *J. Electroanal. Chem.*, 2004, **573**, 175-182.

27 R. P. Akkermans, M. F. Suárez, S. L. Roberts, Q. Fulian and R. G. Compton, *Electroanalysis*, 1999, **11**, 1191-1202.

28 A. Manjavacas, J. G. Liu, V. Kulkarni and P. Nordlander, *ACS Nano*, 2014, **8**, 7630-7638.

29 M. L. Brongersma, N. J. Halas and P. Nordlander, *Nat. Nanotechnol.*, 2015, **10**, 25-34.

30 C. Clavero, *Nat. Photonics*, 2014, **8**, 95-103.

31 X. Wu, E. S. Thrall, H. Liu, M. Steigerwald and L. Brus, *J. Phys. Chem. C*, 2010, **114**, 12896-12899.

32 A. E. Schlather, A. Manjavacas, A. Lauchner, V. S. Marangoni, C. J. DeSantis, P. Nordlander and N. J. Halas, *J. Phys. Chem. Lett.*, 2017, **8**, 2060-2067.

33 S. Licht, V. Cammarata and M. S. Wrighton, *J. Phys. Chem.*, 1990, **94**, 6133-6140.

